Molecular basis for cysteine oxidation by Plant Cysteine Oxidases from *Arabidopsis thaliana*

Qiong Guo[1#], Zhenzhen Chen[2#], Gao Wu[1], Jie Wen[2*], Shanhui Liao[1*], Chao Xu[1*]

[1]Ministry of Education Key Laboratory for Membrane-less Organelles & Cellular Dynamics, Hefei National Laboratory for Physical Sciences at the Microscale, School of Life Sciences, Division of Life Sciences and Medicine, University of Science and Technology of China, 230027 Hefei, P.R. China;

[2]The First Affiliated Hospital of University of Science and Technology of China (Anhui Provincial Hospital), 230000 Hefei, P.R. China

#These authors contributed equally: Qiong Guo, Zhenzhen Chen

*Correspondence: Jie Wen (jiewen@ustc.edu.cn) or

Shanhui Liao (ajsod@mail.ustc.edu.cn) or Chao Xu (xuchaor@ustc.edu.cn)

Keywords: cysteine oxidation; crystal structure; Arg/N-degron; Cys-sulfinic acid; thiazolidine

Abstract

Plant Cysteine Oxidases (PCOs) play important roles in controlling the stability of Group VII ethylene response factors (ERF-VIIs) via N-Arg/degron pathway through catalyzing the oxidation of their N-Cys for subsequent Arginyl-tRNA--protein transferase 1 (ATE1) mediated arginine installation. Here we presented structures of PCO2, PCO4, and PCO5 from *Arabidopsis thaliana* (*At*PCOs) and examined their *in vitro* activity by MS. On the basis of Tris-bound *At*PCO2, we modelled the Cys-bound *At*PCO2 structure and identified key residues involved in N-Cys oxidation. Alanine substitution of potential N-Cys interaction residues impaired the activity of *At*PCO5 remarkably. The structural research, complemented by mutagenesis and mass spectrometry experiments, not only uncovers the substrate recognition and catalytic mode by *At*PCOs, but also sheds light on the future design of potent inhibitors for plant cysteine oxidases.

Introduction

In Animals and plants, different mechanisms are exploited to sense oxygen concentration and regulate gene expression in response to low oxygen stress (hypoxia)[1]. Animals utilizes hypoxia-inducible transcription factor (HIF) to increase the expression levels of growth factors [2], while Plant Cysteine Oxidases (PCOs) play a critical role in oxygen homeostasis by serving as oxygen-sensing proteins[3, 4]. PCOs were found to control the turnover of Group VII ethylene response factors (ERF-VIIs) starting with Met-Cys- (^{1}MC^{2}), via N-degron pathway[4-7]. Once the N-terminal Met (N-Met) of target protein is excised by Met amino peptidase[8], the exposed N-terminal Cys (N-Cys) is subject to oxidization by PCOs, which covert the Cys to Cys-sulfinic acid ($CysO_2$)[7]. After the oxidation of N-Cys, Arginyl-tRNA--protein transferase 1 (ATE1) installs an arginine before N-$CysO_2$ to promote the proteasomal degradation through the Arg/N-degron pathway[4, 7].

The activity of PCOs were greatly compromised in the hypoxic condition, which promotes the expression of hypoxia-response genes by increasing the *in vivo* stability of the ERF-VIIs it mediated[5, 9]. Five ERF-VII family members were identified in *Arabidopsis thaliana*, including *At*RAP2.2, *At*RAP2.3, *At*RAP2.12, *At*HRE1, and *At*HRE2[5, 10]. The turnovers of above response factors mediated by PCOs provide a new layer in understanding how gene expression during stress response is regulated in a oxygen-dependent manner.

PCOs from *Arabidopsis thaliana* (*At*PCOs) has been found to catalyze the N-Cys oxidization of *At*HRE1 (^{2}CGGAVIS^{8}), *At*HRE2 (^{2}CGGAIIS^{8}), and *At*RAP2.2 (^{2}CGGAIIS^{8}), *etc* [6, 10]. Despite their important biological functions in response to low-oxygen stress, how PCOs recognize the substrate and catalyze the subsequent N-Cys oxidation remain elusive because they display low sequence identity with the dioxygenases that have known structures. Here we solved several crystal structures of PCOs from *Arabidopsis thaliana* (*At*PCOs), including those of *At*PCO2, *At*PCO4, and

*At*PCO5. Although the three PCOs belong to two subfamilies, they display conserved catalytic pocket, suggesting the conserved catalytic mechanism among PCOs. Specifically, the structure of Tris-bound *At*PCO2 allows us to model an N-Cys in the catalytic pocket, which reveals the N-Cys specific recognition by PCOs. The PCOs-mediated N-Cys oxidization was complemented by mass spectrometry (MS) experiments. Therefore, our structure research not only provides structural insights into the N-Cys catalytic mechanism by PCOs, but also sheds light on the future design of chemical inhibitors in interfering with the activities of PCOs.

Results

*At*PCO2, *At*PCO4, and *At*PCO5 exhibit activities towards peptides derived from ERF-VII family members

To study the activities of *At*PCOs *in vitro* systematically, we cloned, expressed and purified the full-length or core fragment of several *At*PCOs, including *At*PCO2$_{48\text{-}276}$, *At*PCO4$_{1\text{-}241}$, and *At*PCO5$_{1\text{-}242}$ (**Fig. 1A**). Then we synthesized two peptides derived from *At*HRE1 and *At*RAP2.2, *At*HRE1$^{2\text{-}10}$ and *At*RAP2.2$^{2\text{-}8}$, Respectively, and examine the activities of *At*PCOs towards the two peptides by MS experiments.

Consistent with previous reports about the control experiments[5, 11], after long incubation without enzyme, the peptides either dimerized via N-Cys (**Fig. 2A and 3A**) or formed thiazolidine (**Fig. 2B and 3B**). The dimerized peptide and formation of thiazolidine were confirmed by the peaks correspond to the ~2-fold molecular weight and the +12 Da, respectively. In contrast, both peptides were efficiently catalyzed by *At*PCO2$_{48\text{-}276}$, *At*PCO4$_{1\text{-}241}$, and *At*PCO5$_{1\text{-}242}$ in 30 minutes at 37˚C, which generated a peak of +32 Da (**Fig. 2C-2E, and Fig. 3C-3E**)

Crystal structure of *At*PCO5$_{1\text{-}242}$, *At*PCO4$_{1\text{-}241}$, and *At*PCO2$_{48\text{-}276}$

To understand the substrate binding and catalytic mechanism of *At*PCOs, we solved the crystal structure of selenomethionine (SeMet) *At*PCO5$_{1\text{-}242}$ at a resolution of 2.50 Å (**Table 1**). Most residues of *At*PCO5$_{1\text{-}242}$ are visible except the residues at N-, C-

terminus or some loop regions owning to internal flexibility (**Fig. 1B**). *At*PCO5 adopts a jelly roll-like fold with a chamber constituted by two β-sheets, β14-β1-β2-β9-β4-β7 and β6-β5-β8-β3, with the former β-sheet packed against α1-α3 (**Fig. 1B, 1C**). There is a long bended insertion between β9 and β14 consisting of β10-β13, in which β10 and β11 form anti-parallel strands with β13 and β12, respectively. Before crystallization, we added excess ferrous ion in the buffer and the density map of a ferrous ion is found in the catalytic center, which is chelated to His98, His100, His164, and three water molecules. His98 and His100 reside in the loop between β3 and β4, while His164 is localized in β8 (**Fig. 1**).

Next we solved structures of *At*PCO4$_{1\text{-}241}$ and *At*PCO2$_{48\text{-}276}$, at resolutions of 2.44- and 1.56- Å, respectively (**Fig. 4A, 4B and Table 1**). Both *At*PCO4 and *At*PCO2 adopt jelly roll-like fold (**Fig. 4A, 4B**). Superposition of three *At*PCO structures show that their overall architecture are very similar, as evidenced by the root-mean-square deviations (RMSDs) in a range of 0.57-0.81 Å (**Fig. 4C**). Especially the three histidines that are chelated to the ferrous ion are conserved in three structures, as an indicative of the conserved ferrous ion chelation mode in *At*PCOs (**Fig. 4A, 4B**). On the basis of sequence alignment, it is very likely that above $(His)_3$ chelation mode also applies for their human homolog, 2-aminoethanethiol dioxygenase (ADO) (**Fig. 1A**).

Intriguingly, in the structure of *At*PCO2, we found that a Tris molecule, mimic of the N-Cys, occupies the catalytic pocket. In the Tris-bound structure, besides the three histidines, the central ferrous ion is also chelated to the nitrogen and the two carboxyl groups of the Tris molecule to complete the six coordination (**Fig. 4D**). The nitrogen group of Tris is hydrogen bonded to the hydroxyl group of the *At*PCO2 Tyr215. Tris also makes van del Walls interactions with Phe123, Ile131, Phe199, and Asp209 of *At*PCO2 (**Fig. 4D**).

Modeled structure of Cys-bound *At*PCO2

Given the similarity between the Tris and the apo cysteine, we modeled the Cys-bound

structure of *At*PCO2 on the basis of the Tris-bound structure and compared its Cys recognition mode with that of recently solved Cys-bound human CDO (PDB ID: 6N42)[12]. Despite the similar architecture and Ferrous ion chelation mode, the jelly-roll fold of CDO deviates remarkably from that of *At*PCO2 (**Fig. 5A**). At the catalytic center, the modelled Cys is chelated to the Fe^{2+} via its main chain amino and side chain thiol groups, similar to that observed in the structure of Cys-bound CDO (**Fig. 5B, 5C**). Despite the similarity, their Cys recognition and catalytic modes are different in several aspects. Firstly, Cys93 and Tyr157 of CDO forms the cysteinyltyrosine bridge to increase the catalytic efficiency (**Fig. 5B**) [12, 13], whereas the crosslinked moiety is not found in any of *At*PCO structures (**Fig. 5C**). Secondly, the nitrogen group of Cys in the Cys-CDO complex is free, whereas the nitrogen group of Cys is hydrogen bonded to the side chain of Tyr215 in the modeled *At*PCO2 complex (**Fig. 5B, 5C**). Thirdly, in both structures, the Cys interaction residues in two structures are distinct (**Fig. 5B, 5C**). In the CDO structure, the Cys makes van der Waals interactions with the side chains of Leu75, Ser83, Val142, and His155 (**Fig. 5B**). In the modelled complex structure of *At*PCO2, the Cys makes van der Waals interactions with the side chains of Phe123, Ile131, and Phe199 of *At*PCO2 and its side chain makes one hydrogen bond with the side chain carboxyl group of Asp209, positioning the Cys in a favorable conformation for oxidation (**Fig. 5C**).

The Cys interaction residues of *At*PCO2 are absolutely conserved in *At*PCO4 and *At*PCO5 (**Fig. 1A**), suggesting a common Cys recognition and catalytic mode shared by *At*PCOs. The counterparts of *At*PCO2 Asp209 and Tyr215 in *At*PCO5 are Asp176 and Tyr182, respectively (**Fig. 1A**). We then generated several single mutants for *At*PCO5$_{1-242}$, including H164A, D176A, Y182F and C190A, and examined their activities towards the peptide RAP2.2$^{2-8}$ (CGGAIIS). MS data show that while H164A abolished the activity by disrupting the ferrous chelation, both D176A and Y182F demonstrated compromised activities towards the *At*HRE1$^{2-10}$ and *At*RAP2.2$^{2-8}$ peptides than wild type *At*PCO5. In contrast, C190A exhibit comparable activity towards the substrate peptide as the wild type (**Supplementary Fig. S1**). Collectively,

the mutagenesis experiments and MS data further confirmed the key roles of the Cys binding residues in cysteine oxidation.

Discussion

Previous work on human CDO reveal that an cysteinyltyrosine bridge is formed to lower the oxidation potential of tyrosine for efficient catalysis[12, 13]. Whether cysteinyltyrosine bridge is also formed in human ADO and PCOs remains unknown because of the absence of structure evidence. By analyzing the structure of *At*PCOs, we proposed that although Cys190 of *At*PCO2 is spatially adjacent to Tyr215 and Tyr225 and the three residues are absolutely conserved in the structures of *At*PCO4 and *At*PCO5 (**Fig. 6**), it could not form the cysteinyltyrosine bridge with either of them. Firstly, the the cysteinyltyrosine bridge of CDO (Cys93-Tyr157) does not have a spatial counterpart in *At*PCO2. The Cys190 of *At*PCO2 is not the counterpart of CDO Cys92 in CDO **(Fig. 5B, 5C**). Secondly, the aromatic ring of *At*PCO2 Tyr225 is far from the thiol group of Cys223, implied that they are not likely to form crosslinked moiety. (**Fig. 6**). Thirdly, as for the Tyr215 of *At*PCO2, it is not likely to cross link with Cys223, either, because its aromatic ring of Tyr215 is parallel to the side chain plain of Cys223 and it would be energetically unfavorable for the Try215 to rotate its aromatic right at least ~90 degree to form cysteinyltyrosine bridge. Also the main chain carbonyl group of Pro214 and the main chain amino group of Ser216 are hydrogen bonded to the side chain of Arg221 and the main chain carbonyl group of Arg221, respectively (**Fig. 6**), which does not allow the Tyr215 main chain to endure remarkable change. Above mentioned spatial pattern of the Cys223, Tyr215, and Tyr225 of *At*PCO2 are also conserved in *At*PCO4 and *At*PCO5 (**Fig. 6**), suggesting that *At*PCOs probably exploit a different mechanism rather than cysteinyltyrosine bridge to catalyze cysteine oxidation. We further mutating the Cys190 of *At*PCO4, the counterpart of the *At*PCO2 Cys223, to an Ala, and found that C190A does not impair the *At*PCO4 activity towards RAP2.2$^{2-8}$ (**Supplementary Fig. S1**).

During the preparation of the manuscript, the structures of *At*PCO4 and *At*PCO5 from

Arabidopsis thaliana were reported[14]. In that study, the presented structures, as well as the conclusions drawn on the basis of the structures, are similar to ours. In near future, the substrate- or inhibitor- bound structures of *At*PCOs would further uncover the catalytic mechanism of N-Cys oxidation.

Conclusion

Plant Cysteine Oxidases from Arabidopsis thaliana have been reported to play an important role in controlling the turnover of response factors via Arg/N-degron pathway. Our presented structures of *At*PCO2, *At*PCO4, and *At*PCO5 unraveled the architecture of PCOs, and the structure of ligand-bound *At*PCO2 revealed the potential substrate binding and oxidation residues in the catalytic pocket. Besides, sequence alignment indicates that human ADO might utilize a mechanism to catalyze the oxidation of N-Cys similar to those of *At*PCOs. Overall our research not only provides insight into the N-Cys oxidation mechanism by PCOs, but also sheds light on the design of inhibitors for PCOs.

Acknowledgements: We thank the staff at beam line BL18U1 of the Shanghai Synchrotron Radiation Facility for providing technical support and assistance in data collection and analysis. This work was supported by the “Strategic Priority Research Program” of the Chinese Academy of Sciences (Grant No. XDB19000000) and National Natural Science Foundation of China Grants (31770806, 31500601). C. X. is also supported by the Major/Innovative Program of the Development Foundation of the Hefei Center for Physical Science and Technology (2018CXFX007) and the “Thousand Young Talent program”.

Declarations of interest: The authors declare that they have no conflict of interest

Author contributions: Q.G. and C.X. designed and conceived the study. Q.G., Z.C., S.L. purified, crystallized the protein, solved the structure, and analyzed the data. Q.G. and G.W. performed MS experiments. C.X. wrote the paper with the help from all authors. J.W., S.L., and C.X. supervised the experiments.

Materials and Methods

Cloning, mutation, protein expression and purification

Genes encoding full-length *At*PCO2, *At*PCO4, and *At*PCO5 were synthesized by Sangon Biotech (Shanghai). *At*PCO2$_{48-276}$, *At*PCO4$_{1-241}$, and *At*PCO5$_{1-242}$ was amplified by polymerase chain reactions (PCR), and cloned into pET28-MHL (Genbank accession number: EF456735). The plasmids were then transformed into *E. coli* BL21 (DE3) and the recombinant proteins were overexpressed at 16 ℃ for 20 h in the presence of 0.2 mM isopropyl b-D-1-thiogalactopyranoside (IPTG).

Cells were harvested at 3600 × g, 4 ℃ for 15 min, and then were resuspended using a buffer containing 20 mM Tris-HCl (pH 7.5), 400 mM NaCl (suspension buffer) and were lysed by sonication. Lysates were centrifuged at 18000 × g, 4 ℃ for 30 min and supernatants were collected. Recombinant proteins were purified with a fast flow Ni-NTA column (GE Healthcare) and eluted by 20 mM Tris-HCl (pH 7.5), 400 mM NaCl, 500 mM imidazole. Gel filtration and ion-exchange were employed for further purification. Gel filtration experiments were performed on a HiLoad^{TM} 16/ 600 superdex^{TM} 75 pg column (GE healthcare) with suspension buffer, the fractions containing target recombinant proteins were collected and dialyzed to ion exchange buffer A (20 mM Tris-HCl pH 7.5, 50 mM NaCl). Ion exchange experiments were performed on a Hitrap^{TM} Q HP (1 mL) column (GE healthcare) with ion exchange buffer A and ion exchange buffer B (20 mM Tris-HCl pH 7.5, 1 M NaCl), fraction corresponding to target proteins were collected and concentrated to 20-40 mg/mL and stored at -80℃ before further use. Seleno-Methionine (SeMet)-labeled *At*PCO5$_{1-242}$ was purified in the same way, except that cells were cultured in M9 medium supplied with 50mg/L Seleno-Methionine. The mutants were constructed by conventional PCR using a MutanBEST kit (TaKaRa) and further verified by DNA sequencing. The mutants were expressed and purified in the same way as the wild type proteins.

Crystallization, data collection and structure determination

Before crystallization, recombinant proteins were pre-incubated with Fe^{2+} at a molar ratio of 1:3 at 4 ℃ for 30 min. For crystallization of *At*PCOs, 1 μl protein was mixed with 1 μl crystallization buffer using the sitting drop vapor diffusion method at 18 ℃. SeMet-labeled *At*PCO5$_{1-242}$ was crystallized in a buffer containing 0.1 M MES monohydrate, pH 6.5, 12% (w/v) PEG20000. *At*PCO4$_{1-241}$ was crystallized in a buffer containing 0.1 M Sodium citrate tribasic dehydrate, pH 5.0, 0.2 M Ammonium acetate, and 20% (w/v) PEG 3350. *At*PCO2$_{48-276}$ was crystallized in a buffer containing 0.1 M Tris hydrochloride, pH 8.5, 0.2 M sodium acetate, and 30% w/v polyethylene glycol 4000. Before flash-freezing crystals in liquid nitrogen, all crystals were soaked in a cryo-protectant consisting of 90% reservoir solution plus 10% glycerol.

The diffraction data were collected on beam line BL18U1 at the Shanghai Synchrotron Facility (SSRF). Data sets were collected and processed using the HKL3000 program[15]. The initial model of SeMet *At*PCO5$_{1-242}$ was solved by CRANK2[16], built manually by COOT[17] and refined by Phenix[18]. The structures of *At*PCO2$_{48-276}$ and *At*PCO4$_{1-241}$ were solved by molecular replacement by using the structure of SeMet AtPCO5$_{1-242}$ as the search model. The structures were built manually by Coot[17] and were further refined by Phenix [18].

The atomic coordinates and structure factors of *At*PCO2, *At*PCO4, and *At*PCO5 have been deposited in the Protein Data Bank with PDB ID codes 7CHJ, 7CHI, and 7CXZ.

Mass spectrometry experiments

Reversed-phase microcapillary/tandem mass spectrometry (LC/MS/MS) was performed using an Easy-nLC nanoflow HPLC (Proxeon Biosciences) with a self-packed 75 mm 15 cm C18 column connected to a QE-Plus (Thermo Scientific) in data-dependent acquisition and positive ion mode at 300 nL/min. Passing MS/MS spectra were manually inspected to ensure that all b-and y-fragment ions aligned with the assigned sequence and modification sites. A 25 μl reaction mixture contained 1 μM *At*PCO2/4/5 (final concentration) and 50 μM peptide (final concentration) in a buffer containing 20 mM Tris-HCl (pH 8.0), 20 mM NaCl, 20 μM $FeSO_4$, 5 mM TCEP, and

1 mM Ascorbic acid. The reaction was incubated at 37˚C for 30min at atmospheric oxygen before being quenched (at 70˚C for 10–15 mins). Then, the tubes were centrifuged at 15000 × g for 10 min. Supernatants were analyzed by LC-MS/MS and Proteomics Browser software, with the relative abundances of substrate and product reflecting the cysteine oxidation activities of proteins.

References

1 Majmundar, A. J., Wong, W. J. and Simon, M. C. (2010) Hypoxia-inducible factors and the response to hypoxic stress. Mol Cell. **40**, 294-309

2 Kaelin, W. G., Jr. and Ratcliffe, P. J. (2008) Oxygen sensing by metazoans: the central role of the HIF hydroxylase pathway. Mol Cell. **30**, 393-402

3 Masson, N., Keeley, T. P., Giuntoli, B., White, M. D., Puerta, M. L., Perata, P., Hopkinson, R. J., Flashman, E., Licausi, F. and Ratcliffe, P. J. (2019) Conserved N-terminal cysteine dioxygenases transduce responses to hypoxia in animals and plants. Science. **365**, 65-69

4 Dissmeyer, N. (2019) Conditional Protein Function via N-Degron Pathway-Mediated Proteostasis in Stress Physiology. Annu Rev Plant Biol. **70**, 83-117

5 White, M. D., Klecker, M., Hopkinson, R. J., Weits, D. A., Mueller, C., Naumann, C., O'Neill, R., Wickens, J., Yang, J., Brooks-Bartlett, J. C., Garman, E. F., Grossmann, T. N., Dissmeyer, N. and Flashman, E. (2017) Plant cysteine oxidases are dioxygenases that directly enable arginyl transferase-catalysed arginylation of N-end rule targets. Nat Commun. **8**, 14690

6 White, M. D., Kamps, J., East, S., Taylor Kearney, L. J. and Flashman, E. (2018) The plant cysteine oxidases from Arabidopsis thaliana are kinetically tailored to act as oxygen sensors. J Biol Chem. **293**, 11786-11795

7 Varshavsky, A. (2019) N-degron and C-degron pathways of protein degradation. Proc Natl Acad Sci U S A. **116**, 358-366

8 Ye, Q. Z., Xie, S. X., Ma, Z. Q., Huang, M. and Hanzlik, R. P. (2006) Structural basis of catalysis by monometalated methionine aminopeptidase. Proc Natl Acad Sci U S A. **103**, 9470-9475

9 Licausi, F., Kosmacz, M., Weits, D. A., Giuntoli, B., Giorgi, F. M., Voesenek, L. A., Perata, P. and van Dongen, J. T. (2011) Oxygen sensing in plants is mediated by an N-end rule pathway for protein destabilization. Nature. **479**, 419-422

10 Weits, D. A., Giuntoli, B., Kosmacz, M., Parlanti, S., Hubberten, H. M., Riegler, H., Hoefgen, R., Perata, P., van Dongen, J. T. and Licausi, F. (2014) Plant cysteine oxidases control the oxygen-dependent branch of the N-end-rule pathway. Nat Commun. **5**, 3425

11 Kallen, R. G. (1971) The mechanism of reactions involving Schiff base intermediates. Thiazolidine formation from L-cysteine and formaldehyde. J Am Chem Soc. **93**, 6236-6248

12 Ye, S., Wu, X., Wei, L., Tang, D., Sun, P., Bartlam, M. and Rao, Z. (2007) An insight into the mechanism of human cysteine dioxygenase. Key roles of the thioether-bonded tyrosine-cysteine cofactor. J Biol Chem. **282**, 3391-3402

13 Joseph, C. A. and Maroney, M. J. (2007) Cysteine dioxygenase: structure and mechanism. Chem Commun (Camb), 3338-3349

14 White, M. D., Dalle Carbonare, L., Lavilla Puerta, M., Iacopino, S., Edwards, M., Dunne, K., Pires, E., Levy, C., McDonough, M. A., Licausi, F. and Flashman, E. (2020) Structures of Arabidopsis thaliana

oxygen-sensing plant cysteine oxidases 4 and 5 enable targeted manipulation of their activity. Proc Natl Acad Sci U S A

15 Minor, W., Cymborowski, M., Otwinowski, Z. and Chruszcz, M. (2006) HKL-3000: the integration of data reduction and structure solution--from diffraction images to an initial model in minutes. Acta Crystallogr D Biol Crystallogr. **62**, 859-866

16 Pannu, N. S., Waterreus, W. J., Skubak, P., Sikharulidze, I., Abrahams, J. P. and de Graaff, R. A. (2011) Recent advances in the CRANK software suite for experimental phasing. Acta Crystallogr D Biol Crystallogr. **67**, 331-337

17 Emsley, P. and Cowtan, K. (2004) Coot: model-building tools for molecular graphics. Acta Crystallogr D Biol Crystallogr. **60**, 2126-2132

18 Adams, P. D., Grosse-Kunstleve, R. W., Hung, L. W., Ioerger, T. R., McCoy, A. J., Moriarty, N. W., Read, R. J., Sacchettini, J. C., Sauter, N. K. and Terwilliger, T. C. (2002) PHENIX: building new software for automated crystallographic structure determination. Acta Crystallogr D Biol Crystallogr. **58**, 1948-1954

Table 1 Data collection and refinement statistics

	SeMet *At*PCO5	*At*PCO4	*At*PCO2
Data collection	Beamline SSRF BL18U1	Beamline SSRF BL18U1	Beamline SSRF BL18U1
Radiation wavelength (Å)	0.9792	0.9792	0.9792
Space group	P 4_1 2_1 2	P 1 2_1 1	C 1 2 1
Cell dimensions			
a, b, c (Å)	67.72, 67.72, 128.32	56.62, 51.70, 82.06	91.07, 46.82, 56.13
α, β, γ (°)	90, 90, 90	90, 108.06, 90	90, 100.94, 90
Resolution (Å)	50.00-2.50(2.59-2.50)	50.00-2.45(2.54-2.44)	50.00-1.56(1.59-1.56)
R_{merge}	0.135(1.625)	0.119(0.344)	0.053(0.194)
I / σI	32.6(4.0)	14.2(4.0)	31.9(8.6)
$CC_{1/2}$	0.985(0.894)	0.993(0.941)	0.999(0.968)
Completeness (%)	100.0(100.0)	99.2(94.5)	100.0(100.0)
Redundancy	24.4(21.5)	6.4(5.4)	6.7(6.1)
Refinement			
Resolution (Å)	24.72-2.50	31.14-2.44	25.14-1.56
Number of unique reflections	19650	26952	33140
R_{work}/R_{free}	0.180/0.226	0.205/0.266	0.157/0.185
Number of atoms/B-factor ($Å^2$)			
Proteins	1698/43.3	3525/40.3	1923/15.9
Metal ions	1/17.3	2/31.1	2/10.8
Others	-	13/56.1	8/9.7
Water	62/42.4	94/33.5	263/25.7
RMSD bonds (Å)/angles (°)	0.009/1.02	0.003/0.56	0.009/1.00
Ramachandran Plot favored/allowed/outliers (%)	95.8/4.2/0.0	97.3/2.7/0.0	97.5/2.5/0.0

Values in parentheses are for highest-resolution shell.

Figure legends

Figure 1. Structure of *At*PCO5. (A) Sequence alignment of *At*PCOs and human ADO (*h*ADO). Secondary structures of *At*PCO5 were labelled in blue at the top of aligned sequences. Three Fe^{2+} chelating histidines (His98, His100, and His164), and residues potentially involved in N-Cys recognition are labeled. (B) Overall structure of *At*PCO5$_{1-242}$. *At*PCO5 is colored in blue, with three Fe^{2+} chelating histidines (His98, His100, and His164) shown in sticks. Fe^{2+} and three water molecules are shown in orange and red, respectively. (C) Topology diagram of *At*PCO5, with secondary structures colored in blue.

Figure 2. Mass spectra data of peptide *At*HRE1$^{2-10}$ (CGGAVISDY) catalyzed by *At*PCOs. (A)-(B) Spectra of peptide without enzyme as the controls. Spectra the peptide CGGAIIS oxidized by (C) *At*PCO5$_{1-242}$, (D) *At*PCO4$_{1-241}$, and (E) *At*PCO2$_{48-276}$.

Figure 3. Mass spectra data of peptide AtRAP2.2$^{2-8}$ (CGGAIIS) catalyzed by *At*PCOs. (A)-(B) Spectra of peptide without enzyme as the controls. Spectra the peptide CGGAIIS oxidized by (C) *At*PCO5$_{1-242}$, (D) *At*PCO4$_{1-241}$, and (E) *At*PCO2$_{48-276}$.

Figure 4. Structures of *At*PCO4$_{1-241}$, and *At*PCO2$_{48-276}$. (A) Overall structure of *At*PCO4$_{1-241}$. The structure of *At*PCO4 is shown in red cartoon, with three Fe^{2+} chelating histidines (His98, His100, and His164) shown in sticks. Fe^{2+} and three water molecules are shown in orange and red, respectively. (B) Overall structure of Tris-bound *At*PCO2$_{48-276}$. The structure of *At*PCO2 is colored in cyan cartoon, with three Fe^{2+} chelating histidines (His134, His136, and His197) shown in sticks. Fe^{2+} and Tris are shown in orange and yellow, respectively. (C) Superposition of the structures of *At*PCO2 (cyan), *At*PCO4 (red), and *At*PCO5 (blue). The structures are shown in ribbon, with Fe^{2+} chelation residues shown in sticks. (D) Detailed interactions between Tris and *At*PCO2. Tris is shown in yellow sticks. Fe^{2+} chelating residues and the Tris-binding residues are shown in cyan sticks. Intermolecular hydrogen bond is indicated by black dashes.

Figure 5. Comparison of the catalytic mechanism of *At*PCOs with that of human CDO. (A) Superposition of the structure of *h*CDO (red) with that of *At*PCO2 (cyan). The proteins are shown in ribbon, with Fe^{2+} chelating residues shown in sticks. (B) The catalytic center of Cys-bound *h*CDO, with the Cys and Cys binding residues shown sticks. (C) The catalytic center of Cys-bound *At*PCO2, with the Cys and Cys binding residues shown sticks.

Figure 6. Spatial pattern of Cys223, Tyr215, and Tyr225 of *At*PCO2. Pro214 and Ser216 form main chain hydrogen bonds with Arg221. Fe^{2+} chelating residues, Arg221, Cys223, Pro214-Ser216, Tyr225, as well as their counterparts in *At*PCO4 and *At*PCO5, are shown in sticks.

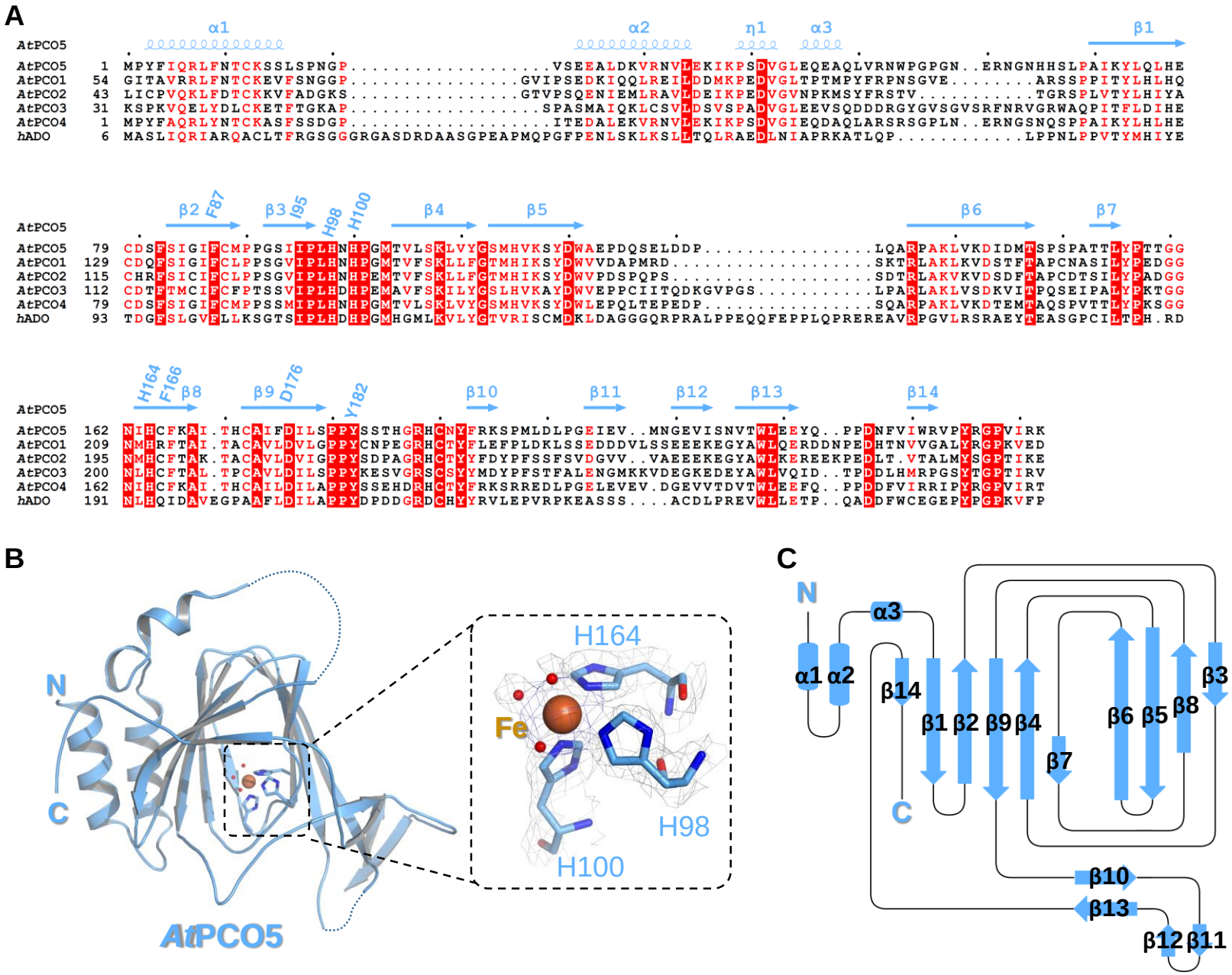
A
α1
α2
η1
α3
β1
AtPCO5
AtPCO5 1 MPYFIQRLFNTCKSSLSPNGP.....VSEEALDKVRNVLEKIKPSDVGLEQEAQLVRNWPGPGN..ERNGNHHSLPAIKYLQLHE
AtPCO1 54 GITAVRRLFNTCKEVFSNGGP.....GVIPSEDKIQQLREILDDMKPEDVGLTPTMPYFRPNSGVE.....ARSSPPITYLHLHQ
AtPCO2 43 LICPVQKLFDTCKKVFADGKS.....GTVPSQENIEMLRAVLDEIKPEDVGVNPKMSYFRSTV.....TGRSPLVTYLHIYA
AtPCO3 31 KSPKVQELYDLCKETFTGKAP.....SPASMAIQKLCSVLDSVSPADVGLEEVSQDDDRGYGVSGVSRFNRVGRWAQPITFLDIHE
AtPCO4 1 MPYFAQRLYNTCKASFSSDGP.....ITEDALEKVRNVLEKIKPSDVGIEQDAQLARSRSGPLN..ERNGSNQSPPAIKYLHLHE
hADO 6 MASLIQRIARQACLTFRGSGGGRGASDRDAASGPEAPMQPGFPENLSKLKSLLTQLRAEDLNIAPRKATLQP.....LPPNLPPVTYMHIYE
β2 F87
β3 I95
H98
H100
β4
β5
β6
β7
AtPCO5
AtPCO5 79 CDSFSIGIFCMPPGSIIPLHNHPGMTVLSKLVYGSMHVKSYDWAEPDQSELDDP.....LQARPAKLVKDIDMTSPSPATTLYPTTGG
AtPCO1 129 CDQFSIGIECLPPSGVIPLHNHPGMTVFSKLLFGTMHIKSYDWVVDAPMRD.....SKTRLAKLKVDSTFTAPCNASILYPEDGG
AtPCO2 115 CHRFSICIFCLPPSGVIPLHNHPEMTVFSKLLFGTMHIKSYDWVPDSPQPS.....SDTRLAKVKVDSDFTAPCDTSILYPADGG
AtPCO3 112 CDTFTMCIFCFPTSSVIPLHDHPEMAVFSKILYGSLHVKAYDWVEPPCIITQDKGVPGS.....LPARLAKLVSDKVITPQSEIPALYPKTGG
AtPCO4 79 CDSFSIGIFCMPPSSMIPLHNHPGMTVLSKLVYGSMHVKSYDWLEPQLTEPEDP.....SQARPAKLVKDTEMTAQSPVTTLYPKSGG
hADO 93 TDGFSLGVFLLKSGTSIPLHDHPGMHGMLKVLYGTVRISCMDKLDAGGGQRPRALPPEQQFEPPLQPREREAVRPGVLRSRAEYTEASGPCILTPH.RD
H164
F166
β8
β9
D176
Y182
β10
β11
β12
β13
β14
AtPCO5
AtPCO5 162 NIHCFKAI.THCAIFDILSPPYSSTHGRHCNYFRKSPMLDLPGEIEV..MNGEVISNVTWLEEYQ..PPDNFVIWRVPYRGPVIRK
AtPCO1 209 NMHRFTAI.TACAVLDVLGPPYCNPEGRHCTYFLEFPLDKLSSEDDDVLSSEEEKEGYAWLQERDDNPEDHTNVVGALYRGPKVED
AtPCO2 195 NMHCFTAK.TACAVLDVIGPPYSDPAGRHCTYYFDYPFSSFSVDGVV..VAEEEKEGYAWLKEREEKPEDLT.VTALMYSGPTIKE
AtPCO3 200 NLHCFTAL.TPCAVLDILSPPYKESVGRSCSYYMDYPFSTFALENGMKKVDEGKEDEYAWLVQID..TPDDLHMRPGSYTGPTIRV
AtPCO4 162 NIHCFKAI.THCAILDILAPPYSSEHDRHCTYFRKSRREDLPGELEVEV.DGEVVTDVTWLEEFQ..PPDDFVIRRIPYRGPVIRT
hADO 191 NLHQIDAVEGPAAFLDILAPPYDPDDGRDCHYYRVLEPVRPKEASSS....ACDLPREVWLLETP..QADDFWCEGEPYPGPKVFP
B
N
C
AtPCO5
H164
Fe
H98
H100
C
N
α3
α1 α2
β14
β1 β2 β9 β4
β7
β6 β5 β8
β3
C
β10
β13
β12 β11

Figure 1

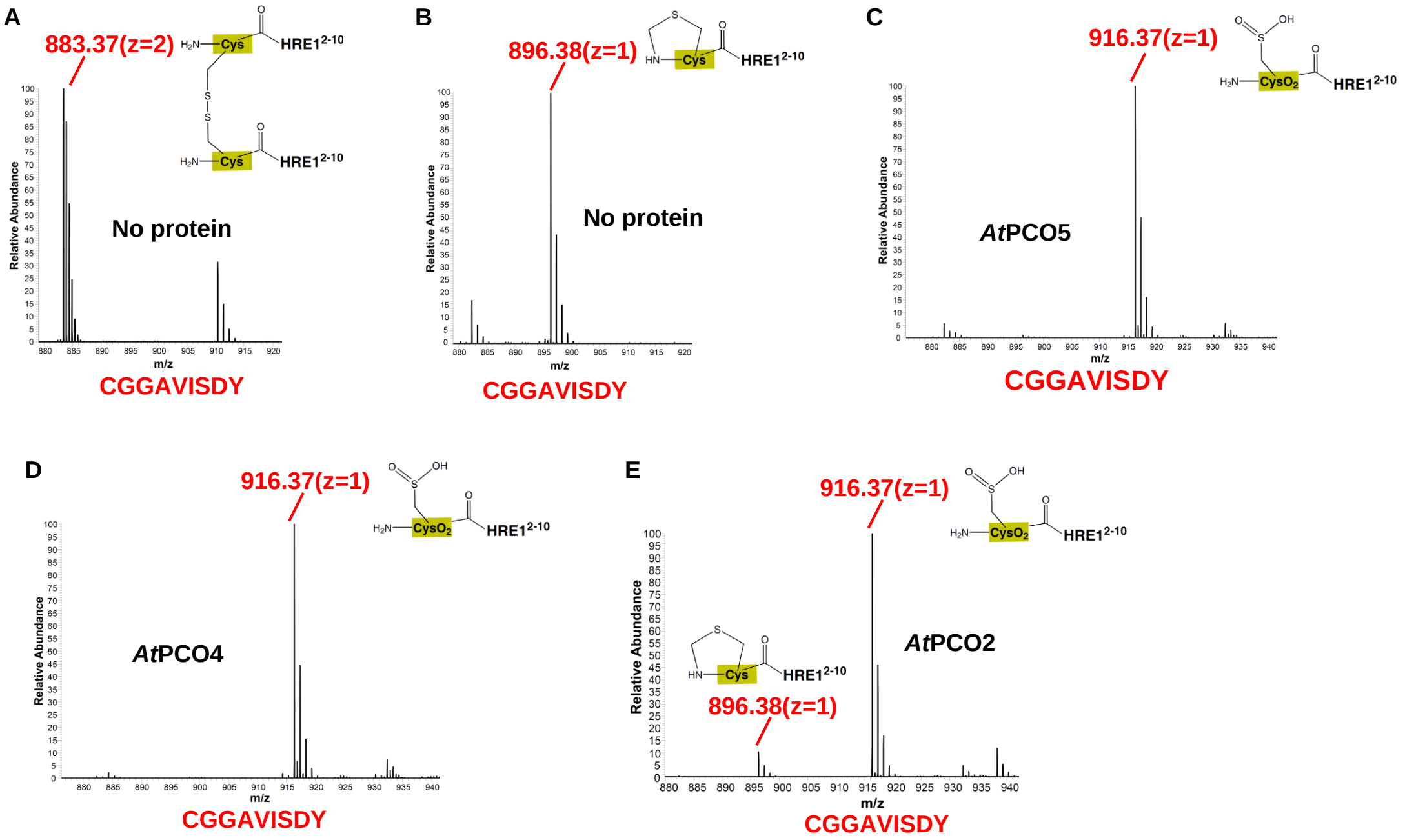
A
883.37(z=2)
Cys
HRE1 2-10
No protein
Relative Abundance
m/z
CGGAVISDY
B
896.38(z=1)
No protein
CGGAVISDY
C
916.37(z=1)
CysO2
AtPCO5
CGGAVISDY
D
916.37(z=1)
AtPCO4
CGGAVISDY
E
916.37(z=1)
AtPCO2
896.38(z=1)
CGGAVISDY

Figure 2

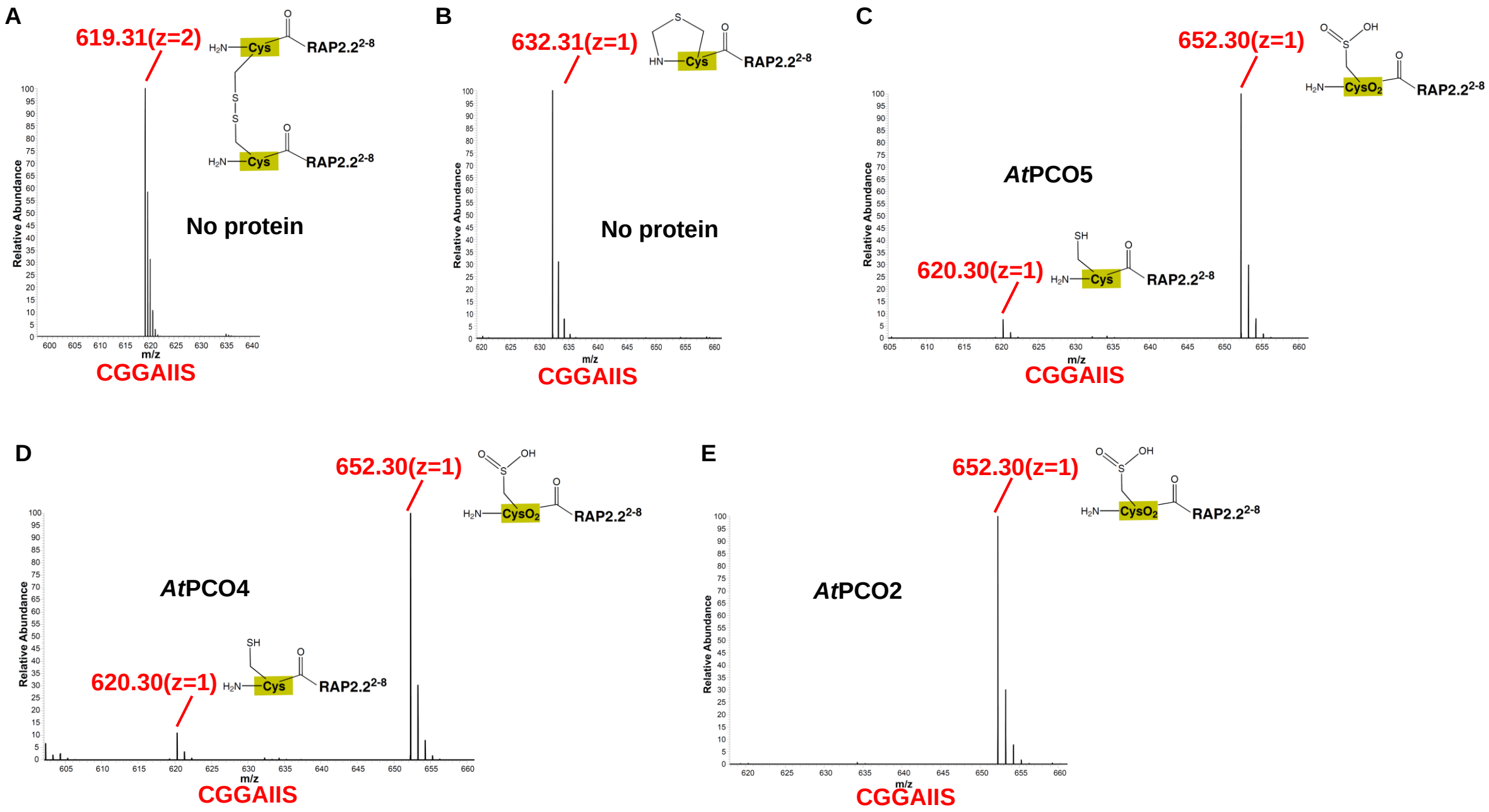
A
619.31(z=2)
No protein
CGGAIIS
B
632.31(z=1)
No protein
CGGAIIS
C
652.30(z=1)
620.30(z=1)
AtPCO5
CGGAIIS
D
652.30(z=1)
620.30(z=1)
AtPCO4
CGGAIIS
E
652.30(z=1)
AtPCO2
CGGAIIS
Relative Abundance
m/z
RAP2.2$^{2-8}$

Figure 3

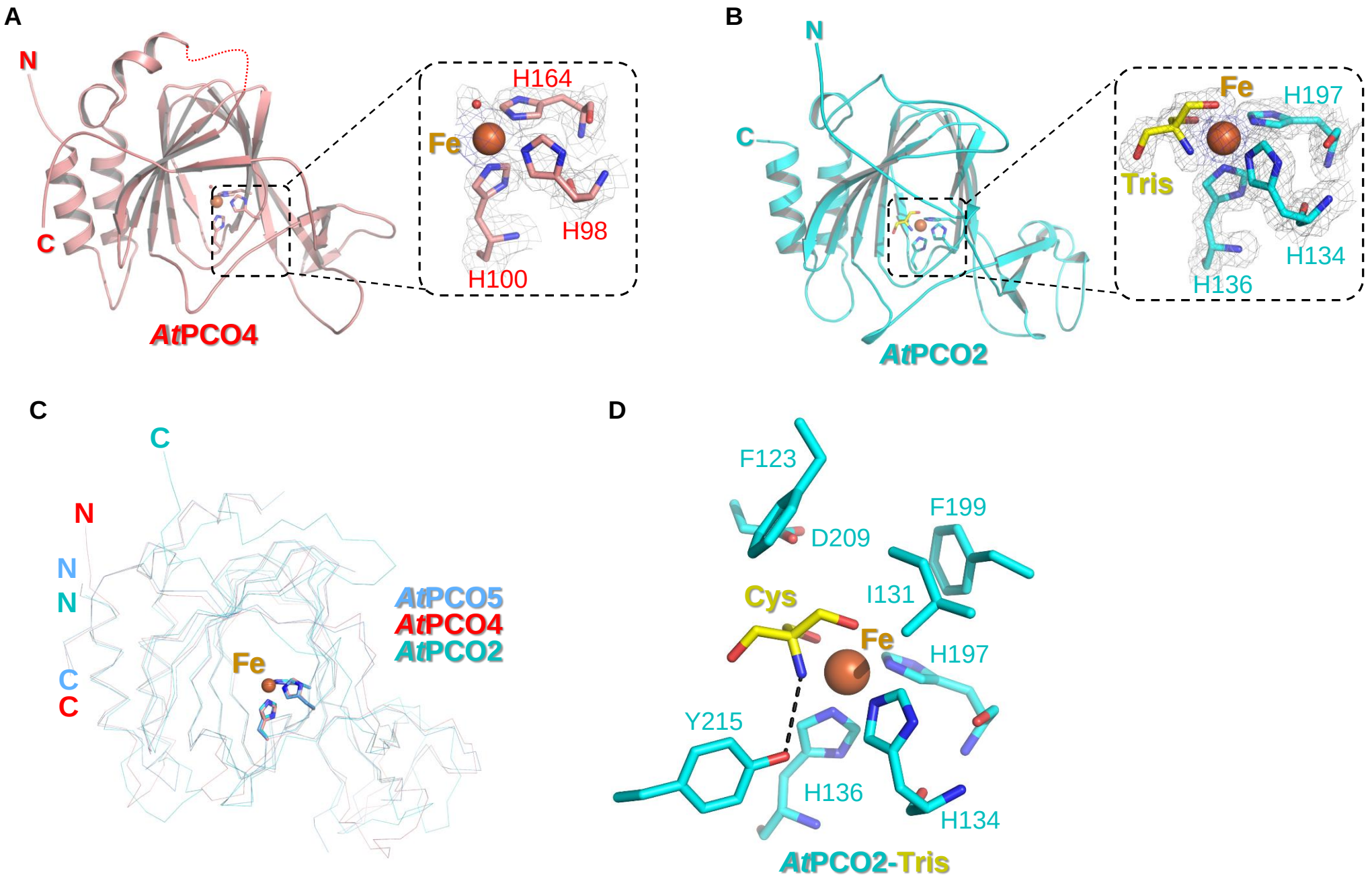
A
N
C
H164
Fe
H98
H100
AtPCO4
B
N
C
Fe
H197
Tris
H134
H136
AtPCO2
C
C
N
N
N
C
C
Fe
AtPCO5
AtPCO4
AtPCO2
D
F123
D209
F199
Cys
I131
Fe
H197
Y215
H136
H134
AtPCO2-Tris

Figure 4

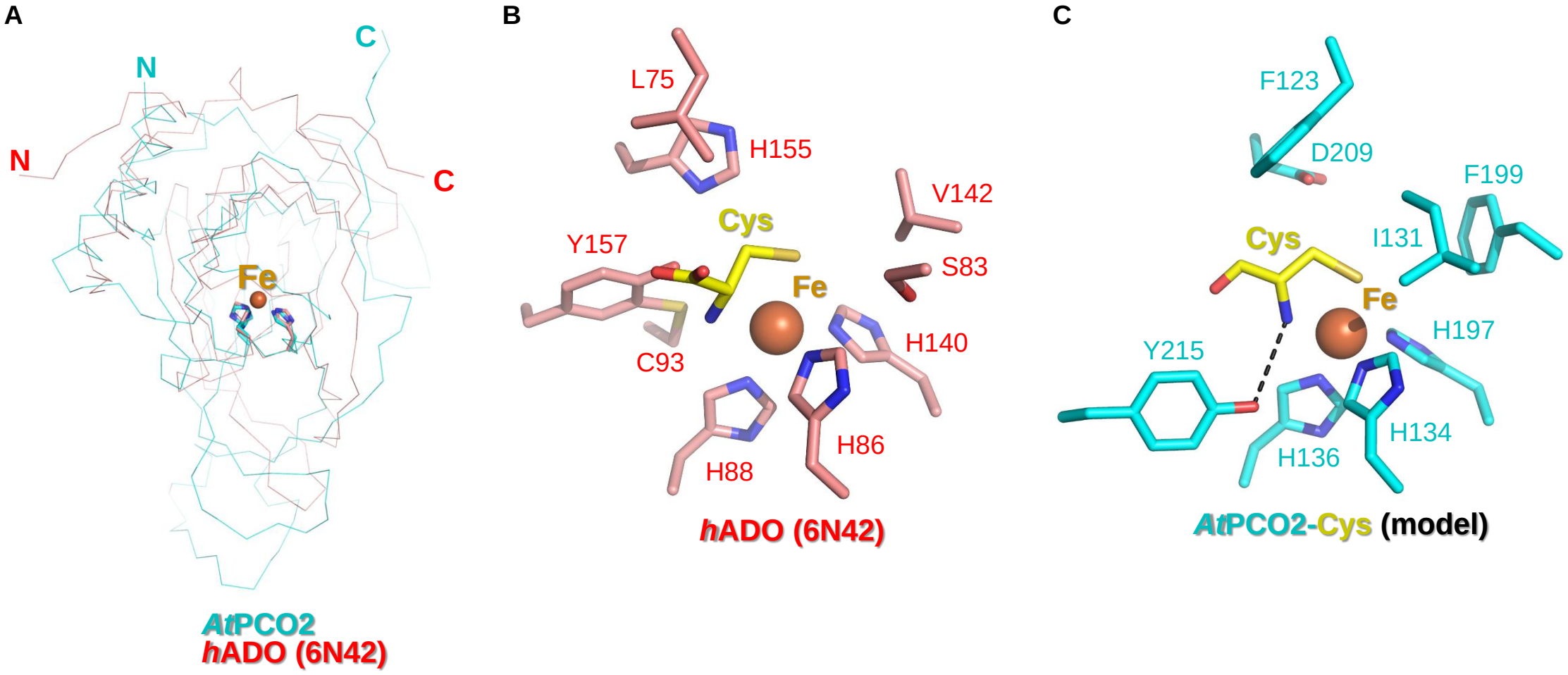
A
N
C
N
C
Fe
AtPCO2
hADO (6N42)
B
L75
H155
V142
Cys
Y157
S83
Fe
H140
C93
H86
H88
hADO (6N42)
C
F123
D209
F199
Cys
I131
Fe
H197
Y215
H134
H136
AtPCO2-Cys (model)

Figure 5

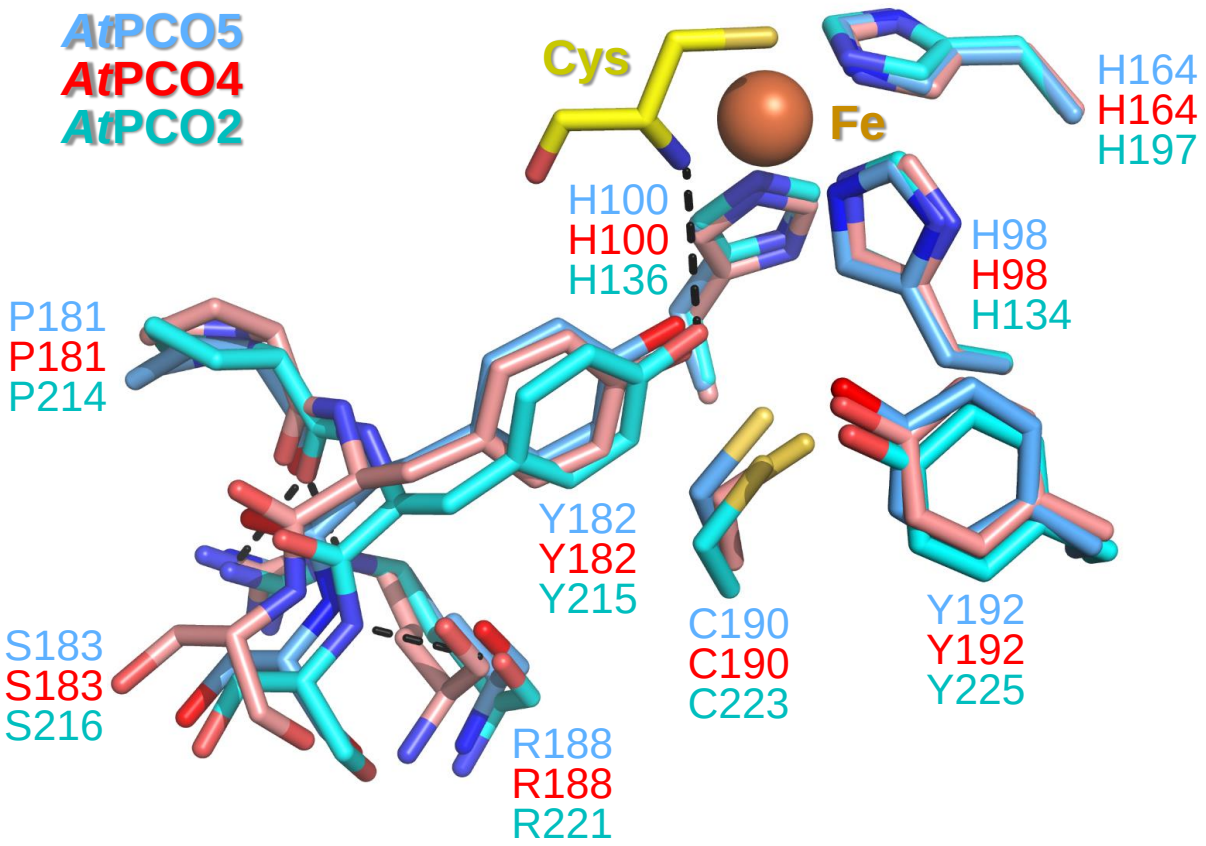
AtPCO5
AtPCO4
AtPCO2
Cys
Fe
H164
H164
H197
H100
H100
H136
H98
H98
H134
P181
P181
P214
Y182
Y182
Y215
C190
C190
C223
Y192
Y192
Y225
S183
S183
S216
R188
R188
R221

Figure 6

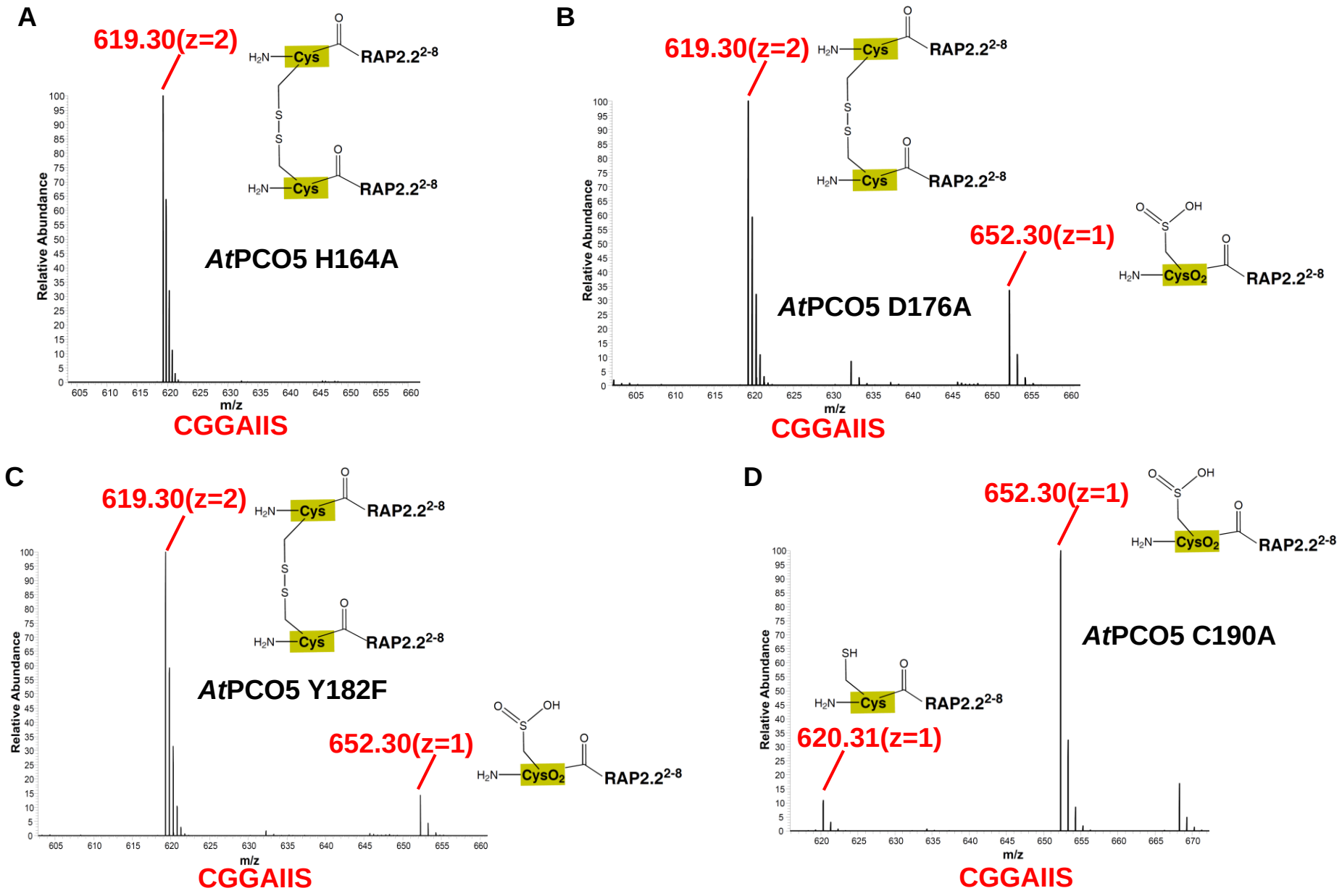

Supplementary Fig. S1. Mass spectra data of peptide AtRAP2.2$^{2-8}$ (CGGAIIS) catalyzed by the variants of *At*PCO5. Spectra of peptide catalyzed by (A) *At*PCO5$_{1-242}$ H164A, (B) *At*PCO5$_{1-242}$D176A, (C) *At*PCO5$_{1-242}$ Y182F, and (D) *At*PCO5$_{1-242}$ C190A.

Supplementary Figure S1